LETTER • OPEN ACCESS

RNA nanopatterning on graphene

To cite this article: Q Li *et al* 2018 *2D Mater.* **5** 031006

View the article online for updates and enhancements.

2D Materials

LETTER

RNA nanopatterning on graphene

Q Li[1,2,4], J P Froning[3,4], M Pykal[3,4], S Zhang[2], Z Wang[2], M Vondrák[3], P Banáš[3], K Čépe[3], P Jurečka[3], J Šponer[3], R Zbořil[3], M Dong[2,5] and M Otyepka[3,5]

1   Key Laboratory Colloid and Interface Chemistry of Ministry of Education, School of Chemistry and Chemical Engineering, Shandong University, Jinan 250100, People's Republic of China
2   Interdisciplinary Nanoscience Center (iNANO), Aarhus University, Aarhus C, DK-8000, Denmark
3   Regional Centre of Advanced Technologies and Materials, Department of Physical Chemistry, Palacký University Olomouc, Olomouc 77146, Czechia
4   These authors contributed equally to this work and should be considered as first authors.
5   Authors to whom any correspondence should be addressed.

E-mail: dong@inano.au.dk and michal.otyepka@upol.cz

Abstract

Graphene-based materials enable the sensing of diverse biomolecules using experimental approaches based on electrochemistry, spectroscopy, or other methods. Although basic sensing was achieved, it had until now not been possible to understand and control biomolecules' structural and morphological organization on graphene surfaces (i.e. their stacking, folding/unfolding, self-assembly, and nano-patterning). Here we present the insight into structural and morphological organization of biomolecules on graphene in water, using an RNA hairpin as a model system. We show that the key parameters governing the RNA's behavior on the graphene surface are the number of graphene layers, RNA concentration, and temperature. At high concentrations, the RNA forms a film on the graphene surface with entrapped nanobubbles. The density and the size of the bubbles depend on the number of graphene layers. At lower concentrations, unfolded RNA stacks on the graphene and forms molecular clusters on the surface. Such a control over the conformational behavior of interacting biomolecules at graphene/water interfaces would facilitate new applications of graphene derivatives in biotechnology and biomedicine.

1. Introduction

Graphene is an amazing 2D material with extraordinary properties such as high sensitivity and low electrical noise, which both have been successfully exploited in sensing and biosensing applications [1–7]. Applications based on the interactions of graphene with biomolecules are especially interesting and potentially useful in drug delivery, detection, DNA sequencing and analysis [6, 8–11], cell-bionic systems, neural signal imaging, and neural prostheses, among other things [12–14]. However, the development of such applications requires a deeper understanding of the interactions of graphene with biomolecules and their building blocks. This will enable the rational design of advanced techniques for, e.g. constructing more effective and sensitive (bio)sensors or optimized connections between graphene and living cells. It is

relevant for biotechnological or medical applications that the analysis of any biomacromolecule's conformational behavior (e.g. proteins and nucleic acids) and their interactions with graphene are based on studies conducted under physiological or near-physiological conditions. At least, such systems must be studied in water at ambient temperature. This requirement regarding the conditions significantly restricts the range of experimental techniques, which can be used to characterize the interaction behavior. Among the available experimental techniques, liquid mode atomic force microscopy (AFM) stands out because of its ability to provide direct nanoscopic insight [15, 16]. The topological information acquired from liquid mode AFM can be further interpreted with the aid of *in silico* molecular dynamics (MD) simulations. Methods for the atomistic MD simulation of biomacromolecules have become

sufficiently mature to provide very useful structural information about the conformational behavior of biomacromolecules [17–19].

Calorimetric experiments show that nucleobases adsorb on graphene and graphite in water environment, with binding affinities decreasing from guanine to thymine (G > A > C ~ T) [20, 21]. Theoretical calculations indicate that the main source of stabilization comes from dispersion interaction (π–π stacking) [22, 23]. It is worth noting that MD simulations suggest that graphene-base interaction is stronger than base-base stacking [24], which implies that nucleic acids may undergo conformational changes upon binding to graphene surface. AFM experiments with single stranded DNA containing thousands of nucleotides show that the DNA molecules adsorb to the graphene surface [25, 26]. However, these experiments were carried out using dried samples and cannot fully reflect behavior of DNA in its native water environment, where solvation/desolvation processes play important role due to the polyanionic nature of DNA. Theoretical calculations explicitly including water environment suggest that DNA can adsorb on the carbonaceous surface [27–30]. AFM experiments with dry single stranded DNA samples confirm that intramolecular stacking in the single strand competes with the π–π stacking to graphene [31]. On the other hand, double stranded DNA does not unfold on graphene [26], however, MD simulations suggest that DNA duplexes may stack on graphene by stem-ending base pairs [32]. It is worth noting that also inorganic polyanionic phosphonic acids form highly oriented domains on graphitic surfaces that are parallel aligned with the surface [33]. Interaction of RNA with graphene surface is unexplored with respect to DNA, despite the fact that short RNAs are gaining more and more attention due to their important biological role in gene expression regulation [34]. In addition, despite all the progress in this field any direct experiment addressing conformational behavior of nucleic acids on graphene in native water environment has not been presented yet.

We analyzed the behavior of 10-nucleotides-long RNA oligonucleotides on graphene surfaces in water. We chose this oligonucleotide because of its structural features: it is an autonomous RNA hairpin that folds in a context-independent manner, has a hydrophobic patch at the bottom of the A-RNA duplex, and contains a GNRA tetraloop tip (figure 1) that serves as a recognition spot in RNA–RNA and RNA-protein interactions [35, 36]. Moreover, hairpins including the GNRA tetraloop sequence exhibit high thermal stability [37, 38].

Our liquid AFM experiments revealed that the behavior of this RNA on graphene is complex and dependent on the RNA concentration, the temperature, and the number of graphene layers. In water, graphene caused the oligonucleotide to unfold; MD simulations indicated that the RNA nucleobases preferentially stacked with the graphene surface. That is,
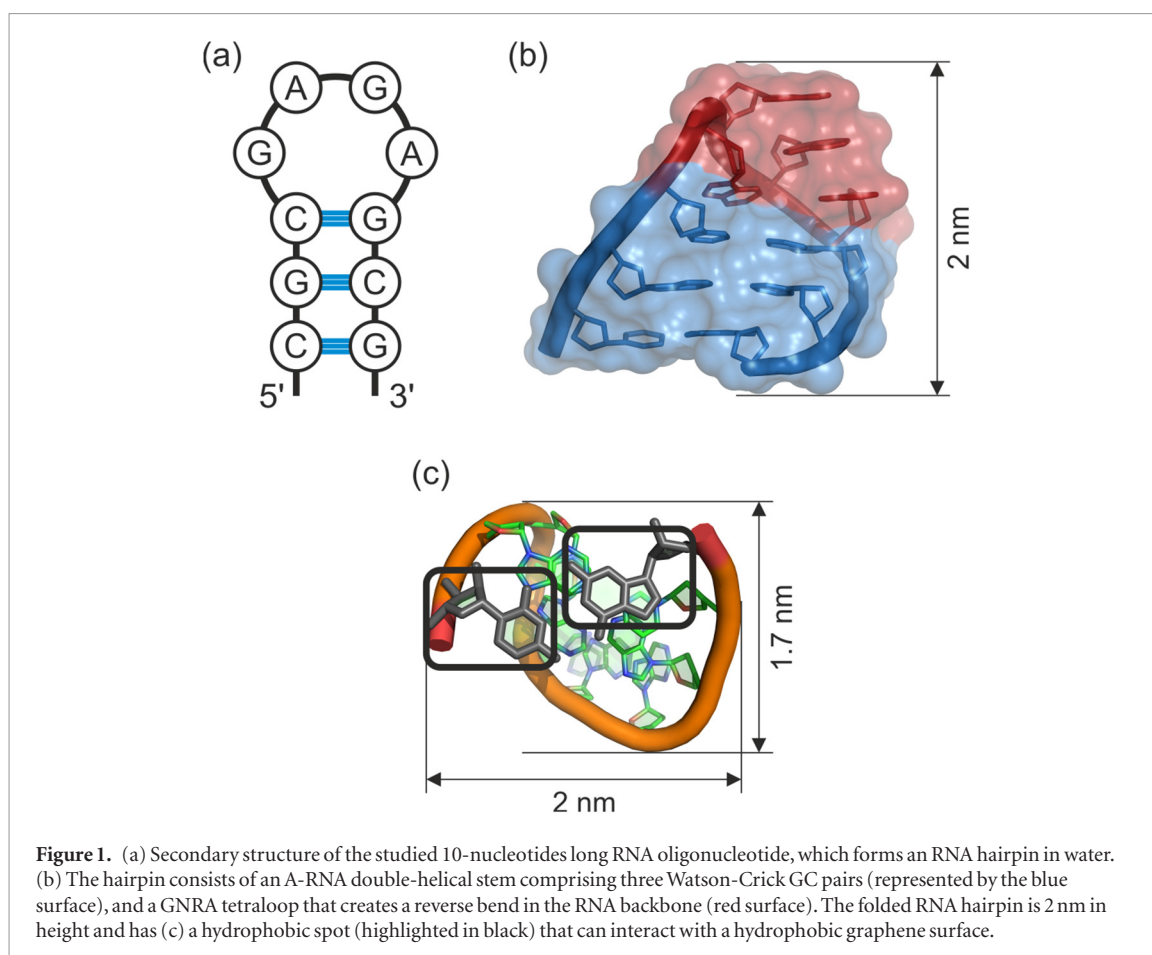
stacking interactions between the graphene surface and nucleobases appeared to outcompete internal interactions within the folded RNA. At higher concentrations, the RNA formed a homogenous uniform film on the graphene surface, entrapping nanobubbles in a self-assembled pattern. The pattern's properties depended on the number of graphene layers. As the number of layers increased, the nanobubbles became larger and more sparsely distributed. These observations clearly demonstrate that a prototypical RNA molecule exhibits complex behavior on graphene surfaces. Such behavior could influence signal harvesting from graphene-based biosensors because the observed unfolding might complicate processes such as the construction of graphene-RNA aptamer-based sensors. Besides the number of graphene layers, additional experiments identified several variables—the biomolecule concentration, temperature, and surface hydrophobicity—through which the behavior of biomolecules on graphene could be manipulated. Systems designed for applications in fields such as drug delivery, gene therapy, or ultrasound imaging would benefit from this degree of control.

2. Methods

2.1. Experimental details

Graphene flakes were prepared by mechanical exfoliation of natural graphite (Alfa Aesar, USA) and deposited on top of a Si substrate with a 300 nm thick SiO_2 layer under normal ambient conditions. The flakes were located by optical microscopy and their identity was confirmed by Raman spectroscopy. The RNA oligo 5′-CGC(GAGA)GCG-3′ (DNA Technology, Denmark) was dissolved in DNA/RNA base-free water (Life Technologies, Denmark) to a concentration of 100 pmol μl^{-1} and stored at −20 °C as 10 μl aliquots. In a typical measurement, 5 μl of RNA solution (100 pmol μl^{-1}) was deposited directly onto the graphene surface on the SiO_2 substrate without further treatment.

All AFM images were recorded using a commercial MultiMode VIII AFM instrument (Bruker, Santa Barbara, USA) operated in tapping mode unless stated otherwise. For AFM imaging in aqueous suspension, 5 μl of RNA solution (100 pmol μl^{-1}) was deposited directly onto the graphene surface on the SiO_2 substrate and incubated for 5 min at room temperature. Then, 40 μl DNA/RNA base-free water was deposited on the surface and liquid AFM was performed using silicon nitride cantilevers (OMCL-TR400PSA-1; Olympus). Immediately before ambient AFM imaging, the sample was dried with nitrogen. AFM imaging in air was performed using ultrasharp silicon cantilevers (OMCL-AC160TS-R3; Olympus) with a nominal spring constant of 26 N m^{-1}. For thermal control, the AFM scanner was equipped with a heating element that served as a suitable platform for the thermal response experiments. The resistive heating stage

Figure 1. (a) Secondary structure of the studied 10-nucleotides long RNA oligonucleotide, which forms an RNA hairpin in water. (b) The hairpin consists of an A-RNA double-helical stem comprising three Watson-Crick GC pairs (represented by the blue surface), and a GNRA tetraloop that creates a reverse bend in the RNA backbone (red surface). The folded RNA hairpin is 2 nm in height and has (c) a hydrophobic spot (highlighted in black) that can interact with a hydrophobic graphene surface.

provides a temperature range from room temperature (RT) to 100 °C with a resolution of 0.1 °C. All the AFM images and size distributions were analyzed using the commercial Scanning Probe Image Processor software package (SPIP, Image Metrology, Denmark).

For electron microscopy, the samples were dispersed in water, sonicated for 5 min and one drop put on copper grid with Holey carbon film. After drying in the air at room temperature were samples measured by high-resolution (HR) transmission electron microscope (TEM) Titan G2 (FEI) with Image corrector on accelerating voltage 80 kV. Images were taken with BM UltraScan CCD camera (Gatan). Energy dispersive spectrometry (EDS) was performed in scanning TEM (STEM) mode by Super-X system with four silicon drift detectors (Bruker). STEM images were taken with HAADF detector 3000 (Fishione).

2.2. Computational details

MD simulations were performed using the Gromacs 4.5.5 package [39] with the Plumed 2.1.1 extension [40]. The initial structure of the folded RNA hairpin tetraloop (TL) was derived from the x-ray structure of the sarcin/ricin loop with PDB ID 1Q9A [41], and was terminated by two and three GC pairs, respectively, to increase the fragment's stability, yielding the sequence 5′-GC(GAGA)GC-3′ and 5′-CGC(GAGA)GCG-3′. The structure of the unfolded state was taken from a high temperature MD simulation [42]. Graphene was

treated as a periodic sheet (resulting in box dimensions of ca. 8.5×8.5 nm) consisting of uncharged Lennard–Jones (LJ) spheres with Cheng and Steele interaction parameters [43]. RNA was modeled using the ff99bsc0χ_{OL3} force field [44] with revised van der Waals (vdW) parameters for phosphate oxygens [45] and an additional potential (HBfix) to improve the description of native hydrogen bonding [46]. Both corrections are crucial for a correct description of RNA and have been shown to provide the correct balance of folded/unfolded states in TL folding [46]. All systems were solvated using the OPC water model [47] and neutralized with Na$^+$ ions [48]. Periodic boundary conditions were applied in the *xyz* dimensions. The particle mesh Ewald (PME) method (with a real space cutoff of 1 nm) was used to model long-range interactions. VdW interactions were truncated at 1 nm. The LINCS algorithm [49] was used to constrain bonds to hydrogen atoms. All MD simulations were performed in the NpT ensemble, using the velocity rescale thermostat [50] and the anisotropic Berendsen barostat for pressure regulation. We considered both folded and unfolded states of the RNA sequence to calculate enthalpy differences corresponding to the folding/unfolding process in water and on graphene (see figure S10 (stacks.iop.org/TDM/5/031006/mmedia) for an overview of the simulation setup). The initial structures used for enthalpy calculations were minimized and thermalized at 300 K and 1 bar with a
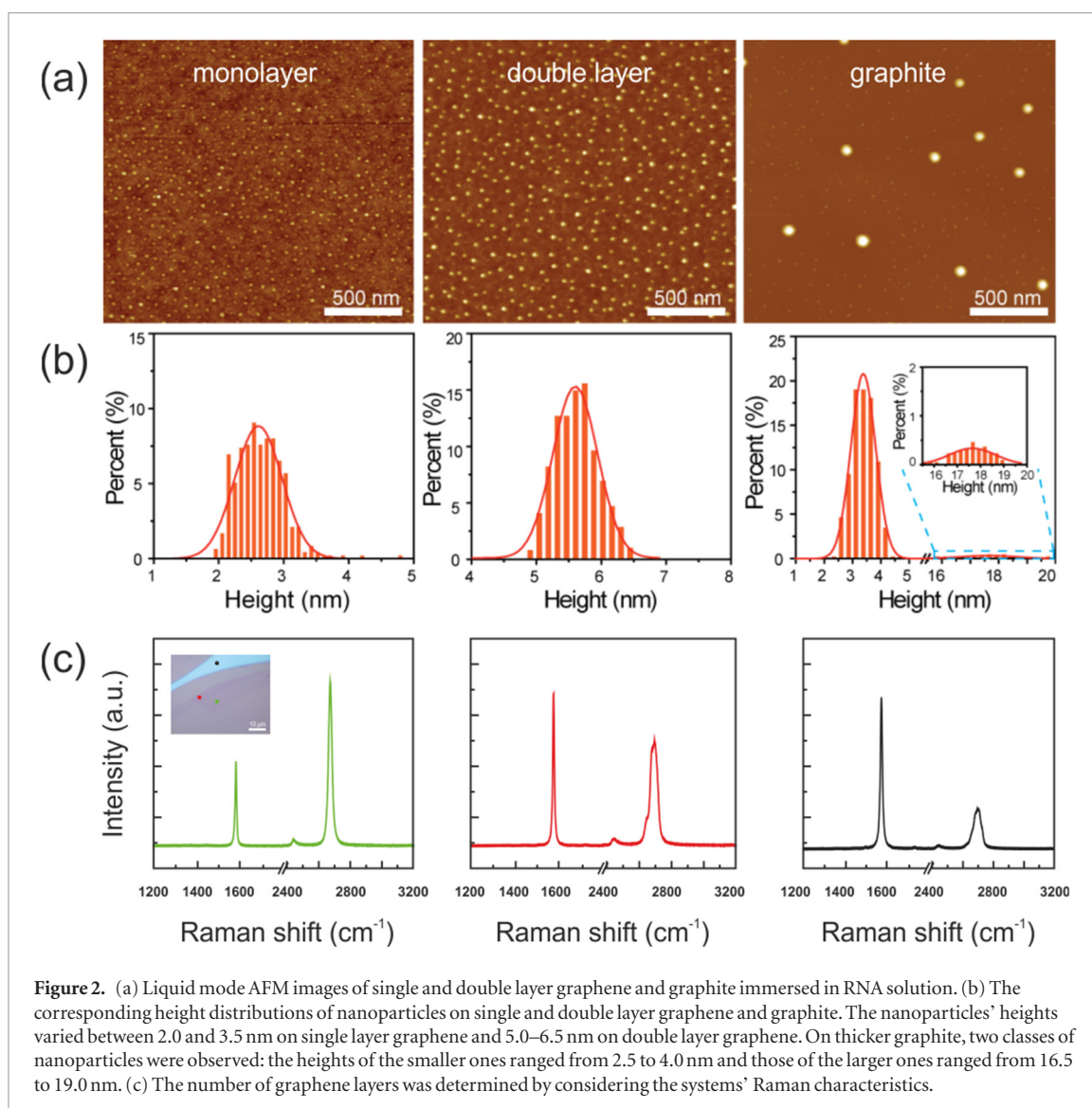
Figure 2. (a) Liquid mode AFM images of single and double layer graphene and graphite immersed in RNA solution. (b) The corresponding height distributions of nanoparticles on single and double layer graphene and graphite. The nanoparticles' heights varied between 2.0 and 3.5 nm on single layer graphene and 5.0–6.5 nm on double layer graphene. On thicker graphite, two classes of nanoparticles were observed: the heights of the smaller ones ranged from 2.5 to 4.0 nm and those of the larger ones ranged from 16.5 to 19.0 nm. (c) The number of graphene layers was determined by considering the systems' Raman characteristics.
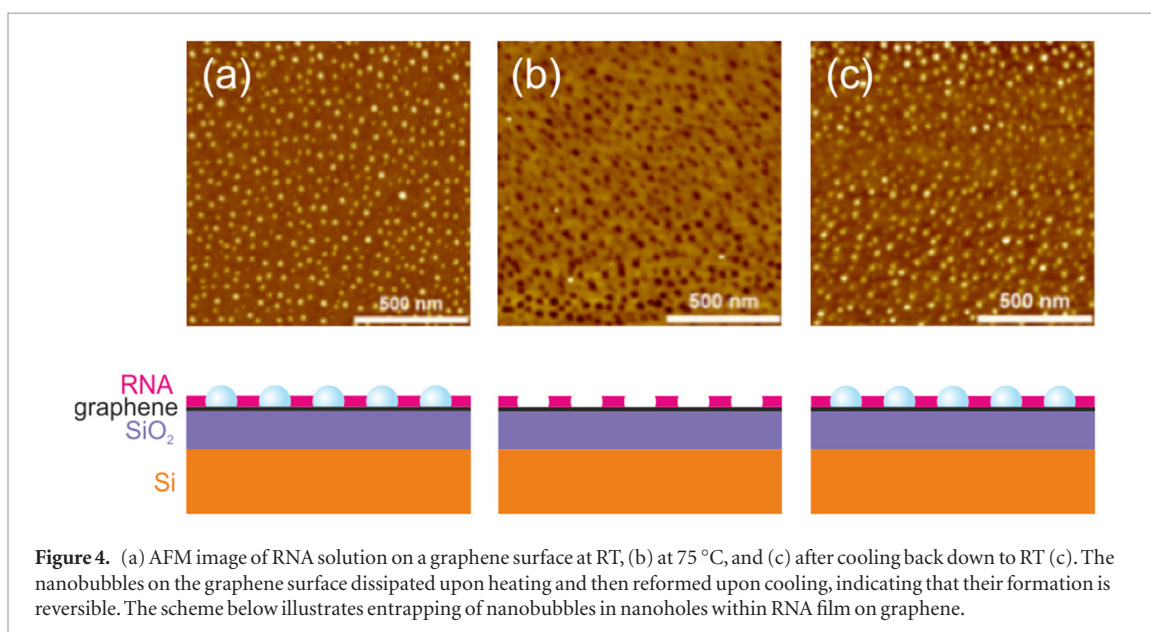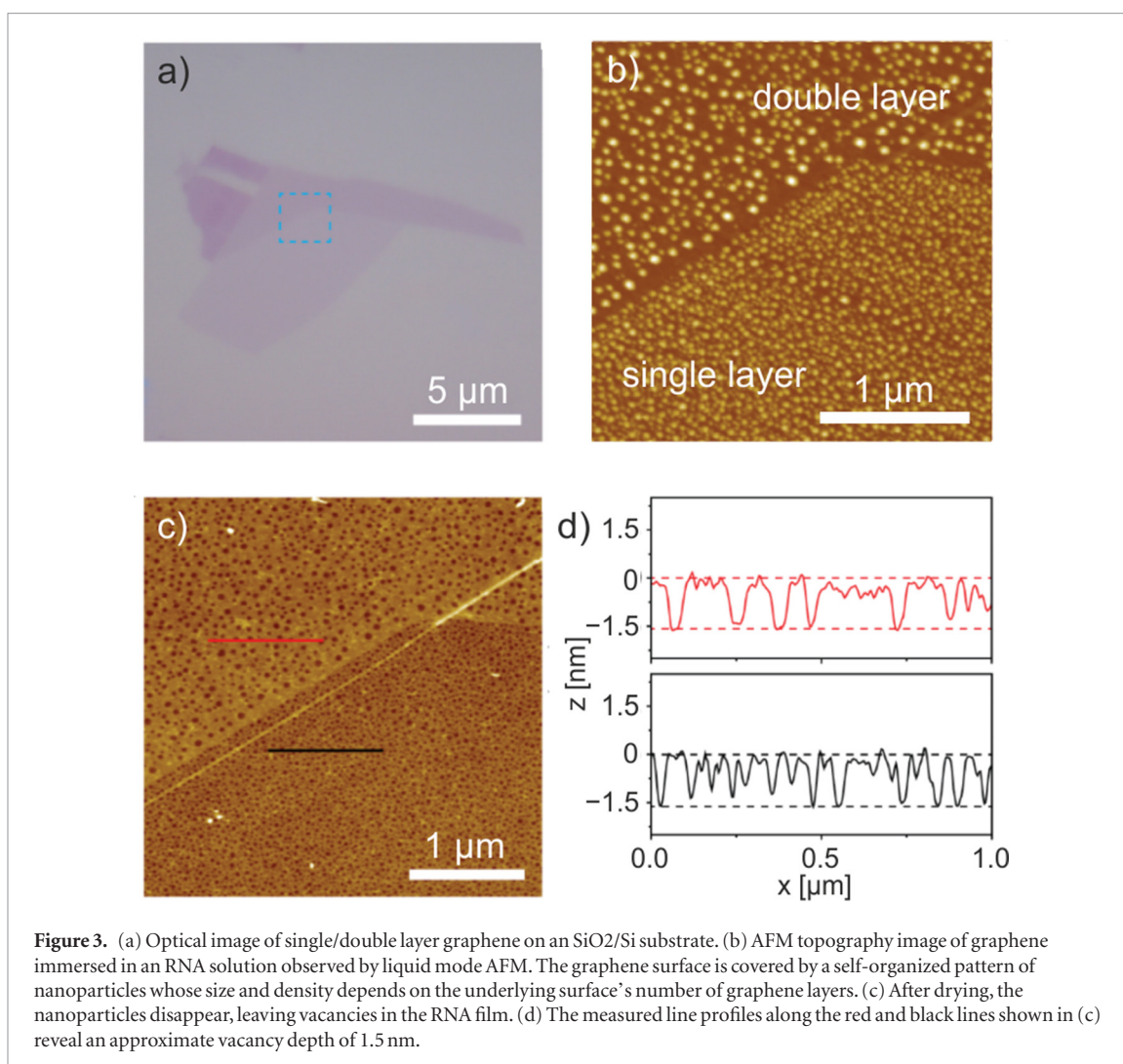
time step of 2 fs, followed by a 400 ns production run, of which the first 100 ns were treated as an equilibration stage and thus excluded from the final analysis. Average enthalpies were obtained using Gromacs' *g_energy* tool. Energy differences were recorded between independent simulations corresponding to different RNA conformations (folded and unfolded) with and without the presence of graphene. A necessary precondition for comparing the results of any two simulations was that they involve the same numbers of atoms of each type. This approach was successfully used by Peréz-Villa *et al* to study RNA/protein complexes [51]. To model RNA association, 9 unfolded 10-mer RNA molecules were placed in the vicinity of a graphene surface (their total net charge was neutralized by adding sodium counter ions) and simulated for 100 ns under the conditions described above.

3. Results

3.1. Self-organized pattern of RNA on the graphene
At the higher concentration of 100 pmol μl^{-1}, the studied RNA oligonucleotide formed a self-organized

pattern of nano-objects on the graphene surface (figure 2). Liquid mode AFM was employed for the topographical measurement and the visualization of the mechanically exfoliated single and double layer graphene and graphite while being immersed in the RNA solution. Further, AFM aided in the identification of the different patterns formed by nano-objects on the graphene/graphite surface (supporting figure S1). The self-organized pattern was rather homogeneously distributed over the graphene surface independent of the layer underneath. The number of layers, however, influenced both size and density of the nanoparticles (figure 2(a)). The height histograms of the particles' dimensions were evaluated for all three substrates, single and double layer graphene and graphite. The average particle height on single layer graphene was 2.6 ± 0.4 nm, while the nanoparticles on graphene bilayers were twice as large on average, 5.6 ± 0.3 nm (figure 2(b)). On graphite, two sizes of objects were observed with average heights of 3.3 ± 0.5 and 17.6 ± 1.1 nm arranged in a sparse network (figure 2(b) and supporting figure S2). Besides the dimension, the densities of the observed particles

Figure 3. (a) Optical image of single/double layer graphene on an SiO2/Si substrate. (b) AFM topography image of graphene immersed in an RNA solution observed by liquid mode AFM. The graphene surface is covered by a self-organized pattern of nanoparticles whose size and density depends on the underlying surface's number of graphene layers. (c) After drying, the nanoparticles disappear, leaving vacancies in the RNA film. (d) The measured line profiles along the red and black lines shown in (c) reveal an approximate vacancy depth of 1.5 nm.

Figure 4. (a) AFM image of RNA solution on a graphene surface at RT, (b) at 75 °C, and (c) after cooling back down to RT (c). The nanobubbles on the graphene surface dissipated upon heating and then reformed upon cooling, indicating that their formation is reversible. The scheme below illustrates entrapping of nanobubbles in nanoholes within RNA film on graphene.

were estimated from the same AFM pictures. As the number of graphene layers increased, the density of nanoparticles on the carbon flakes fell from 187 particles per μm^2 (ppsmi) for single layer graphene to 142 ppsmi for double layer graphene and ended with 104 ppsmi for the smaller particles on graphite. The largest nanoparticles had a density of only 4 ppsmi. In an intermediate conclusion, the nanoparticles' height and average distance to their nearest neighbor seemed both to increase along with the number of graphene layers. The size and density variation of the nano-objects could not have been caused by experimental

conditions since the AFM pictures were taken at the same conditions at separate experiments and it was even observed in a single measurement on different layers (figure 3).

3.2. Nanobubbles entrapped by RNA film on top of graphene

In order to decipher the nature of the observed nano-objects we carried out additional experiments; liquid mode AFM experiments at elevated temperature, AFM experiments under ambient conditions and high-angle annular dark field (HAADF) of scanning transmission electron microscopy (STEM) followed by the elemental mapping by the corresponding energy dispersive x-ray spectroscopy (EDS) on dried samples. In the performed liquid AFM experiments at an elevated temperature, the nanoparticles disappeared upon heating to 75 °C (figure 4) and then reformed upon cooling back to room temperature (RT), indicating a reversible process of formation/disintegration of nano-objects. The well depth of the vacancies observed at 75 °C was 1.5 nm (supporting figure S3). This suggested that the observed nano-objects are not composed of biomolecules, but rather of gas residing at the interface. The higher temperature would cause the disintegration of these bubbles that could originally prevent access of the probe to the graphene surface in the liquid mode AFM. It is worth noting that the self-assembled pattern remained intact at the elevated temperature (figure 4), indicating that the graphene surface was covered with a rather well-packed network of RNA molecules.

Prior to the ambient AFM and STEM measurements, the RNA-graphene samples were dried with a dry nitrogen stream. During the drying process, the nanoparticles disappeared, leaving vacancies at the positions they had occupied, similarly to elevated temperature experiment, and thereby seeming to produce a negative of the previous pattern (figures 3(b) and (c)). The pattern was not a true negative since the remaining holes were 1.5 ± 0.2 nm deep matching the results from the AFM at an elevated temperature regardless of the number of graphene layers (figure 3(d) and supporting figure S4). This led us to the conclusion that the nanoparticles were nanobubbles made up from trapped gas adsorbed at the solid/liquid interface of water and graphene. During the drying process, this interface would disappear and nanobubbles would disintegrate. Similar nanobubbles had been observed in other AFM experiments [52], and their stability was attributed to the encapsulation of a Knudsen gas [53]. With the nanobubbles on one hand and a hole depth of 1.5 nm on the other, we further deduced that the observed pattern was incorporated in a layer of RNA molecules. This would mean, that the RNA molecules cover the entire accessible graphene/graphite surface forming a film on top of the surface. With the exception, where the formation of nanobubbles acts as a mask preventing parts of the graphene to

be covered. Therefore, the holes would already exist in the liquid phase, but not be visible in the AFM pictures because the probe would not penetrate the bubble surface due to a low loading force. And thus, the holes would be first visible in normal ambient conditions after the disintegration of the nanobubbles due to the drying. Such holes had been observed in previous experiments with dry samples of single stranded DNA on graphene [26], however, the mechanism of their appearance was unclear.

Since the SiO_2 substrate was not covered by the RNA film in any of our experiment, the thickness of the RNA/graphene flake could be measured. The obtained value 2.0 ± 0.2 nm agrees fairly well with a sum of RNA layer (1.2 ± 0.2 nm, see below) and single graphene layer (0.3 ± 0.2 nm), considering, moreover, the eventual graphene and SiO_2 roughness. It should be noted that the observed thickness of the RNA layer on graphene in water and in air did not differ significantly.

Additionally, the observed nano-objects were characterized by HAADF in STEM mode of HR-TEM and by the elemental mapping by EDS analysis (supporting figure S6). The elemental mapping identified the presence of phosphorus, carbon and oxygen covering the graphene surface and surrounding nano-objects. Taking these pictures under UHV conditions under an electron beam alters the behavior of RNA, but confirms presence of the RNA film on graphene surface.

3.3. RNA stacks unfolded to graphene surface

However, the formation of the well-packed RNA layer is only possible when there is enough material to form the homogenous film, i.e. if RNA concentration in solution is high enough. We repeated the liquid mode AFM experiment using the single layer graphene and a 50-fold diluted RNA solution ($c(RNA) = 2$ pmol μl^{-1}). Under these conditions, we did not observe the self-assembled pattern discussed above (see figure 2(a)). The lower concentration was not only insufficient to form the homogenous RNA film but also unable to entrap gas nanobubbles on the graphene surface. Even though, we observed randomly and sparsely distributed nanoparticles, we did not see any other alien nano-objects in the system. The observed clusters were exclusively attached to the graphene surface rather than the SiO_2 support (supporting figure S1). We concluded that the nanoparticles were individual RNA molecules and small RNA clusters (remaining intact after drying); whereby average experimental height was 1.2 ± 0.2 nm. Regarding the experiments with higher concentration, this confirmed homogenous RNA layer and bubble hypothesis. Another indicator was that the stiffness mapping revealed that the observed features were softer than the substrate, although a Young's Modulus cannot be calculated due to the small dimensions of the formed objects (supporting figure S7).
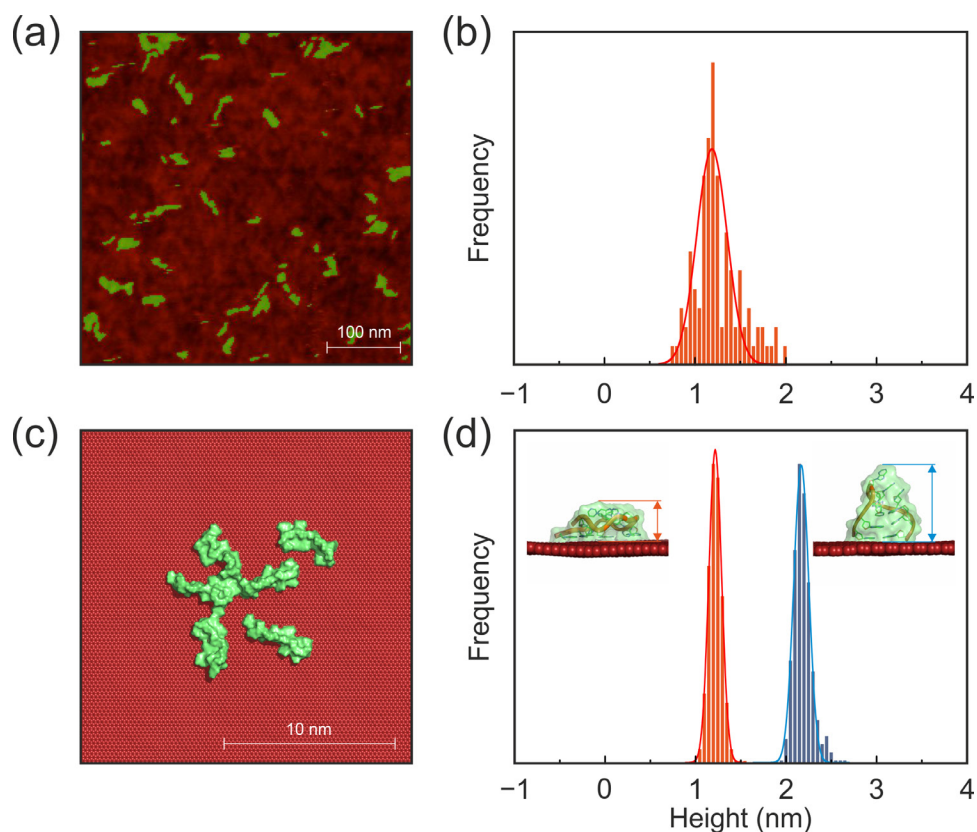
Figure 5. (a) AFM topography image of a small area of the graphene monolayer in a dilute RNA solution, highlighting RNA molecules and clusters in green (original AFM image without the highlighted areas is in figure S9), which were used for the grain analysis resulting in the height histogram shown in panel (b). The mean height of RNA equals to 1.2 ± 0.2 nm, which corresponds to unfolded RNA (see panel (d)) stacking on the graphene surface. (b) Height histogram of distinct RNA molecules or clusters observed on the graphene monolayer by AFM. (c) RNA cluster formed in an MD simulation whose structural features are consistent with the AFM results. The coloring was chosen as in the panel (a) to clearly distinguish between the RNA molecules (in green) and the substrate. (d) Theoretically estimated height histograms of folded (red) and unfolded (blue) RNA molecules on graphene from two independent MD simulations. The insets show representative structures of the unfolded and folded states.

3.4. Theoretical insight into the graphene induced RNA unfolding

To better understand the behavior of RNA molecules on graphene, we performed classical all-atom MD simulations of two differently sized oligonucleotides (10-nucleotides-long and shorter 8-nucleotides-long) in water and computed average enthalpies for its folded and unfolded states. Assuming that hairpin folding is an enthalpy-driven process [54], partly counterbalanced by an unfavorable entropy contribution that is connected with loss of conformational freedom upon hairpin folding (however, in total, the enthalpic contribution exceeds the entropic term), the enthalpy difference can serve for direct comparison of stability of individual RNA states. The simulated oligonucleotides preferentially adopted the folded hairpin conformation in water; the folded form was more thermodynamically stable than the unfolded form by $\Delta H = 15 \pm 1$ kcal mol^{-1} for the 10-nucleotides-long RNA and by $\Delta H = 10 \pm 2$ kcal mol^{-1} for a shorter (8-nucleotides-long) hairpin. Additional GC closing pair in 10-mer hairpin increased the stability of the folded form by approximately $\Delta H = 5$ kcal mol^{-1} compared to 8-nucleotide RNA. This observation is consistent with previous

experimental findings suggesting that the studied oligonucleotide is an autonomously folding hairpin motif that is thermally stable at ambient temperature [55]. These results suggested that the chosen force field and MD simulation setup adequately described the studied system and could be used to help interpret the experimental results. We, therefore, performed additional simulations to study the RNA hairpin's behavior on graphene. The unfolded 10-nucleotides long RNA stacked on the graphene surface was more stable (by $\Delta H = 2 \pm 2$ kcal mol^{-1}) than the folded hairpin interacting with graphene. In the case of the shorter 8-mer hairpin, the enthalpy difference was 11 ± 3 kcal mol^{-1} again in favor of the unfolded form. Moreover, in our simulations practically all bases were directly stacked to the graphene surface. Thus, the unfolded state may be further stabilized by reducing the hydrophobic surface of graphene exposed to water upon base stacking to this surface, i.e. by hydrophobic effect. All this suggests that the hairpin should be expected to unfold in the presence of graphene and bind to the graphene surface via π–π interactions [22]. The average height of the unfolded 10-nucleotide-long RNA on graphene was 1.2 ± 0.1 nm, which is consistent with the height observed in the AFM

experiments with dilute RNA (figures 5(b) and (d)). In another MD simulation with more RNA molecules, we observed the formation of contacts between individual unfolded oligonucleotides on the graphene surface, and the development of RNA clusters (figure 5(c)), which again agreed with the experimental observations. Approximately one half of the bases of individual RNA molecules forming the clusters stacked to the graphene surface and the other half created intermolecular contacts via stacking and hydrogen bonding interactions among RNA hairpins. Each RNA molecule formed ~7 hydrogen bonds with the neighboring RNA hairpins (for more details see supporting figure S8). These noncovalent interactions stabilized RNA clusters on the graphene surface.

Taken together, the experiments and simulations discussed above provide enough evidence that RNA forms stacking interactions with graphene surfaces in water, leading to the development of homogeneous RNA films consisting of clusters of interacting RNA oligonucleotides. These films entrap nanobubbles on the graphene confined by RNA film. Heights and lateral distributions depend on the number of underlying graphene layers. Both height and lateral size of the bubbles might be rationalized by combination of the Young–Laplace and Young equations, although, it is worth to note that the predictability of such macroscopic description is rather limited in case of nanobubbles containing Knudsen gas [53]. In addition, the nanobubbles observed in this study are even one order of magnitude smaller than the nanobubbles stabilized by the Knudsen gas. We hypothesize that the nanobubbles of such small size are stabilized by pinning to the RNA film, which is in turn sensitive to the number of graphene layers because of different hydrophobicity of such surface. The experiments were performed using graphene mounted on a hydrophilic SiO_2 surface. Because graphene exhibits partial wetting transparency [56], the hydrophobicity of the multilayer surface should increase with the number of graphene layers [57]. A corrugation of graphene surface also decreases with number of stacked graphene layers. However, the mechanism governing formation of nanobubbles entrapped in RNA film is not fully elucidated and deserves further analysis.

4. Conclusions

We analyzed the behavior of a prototypical RNA oligonucleotide on graphene in water by liquid mode AFM and interpreted the results with the assistance of all-atom MD simulations. The RNA molecules, which form thermally stable native folded hairpin structures in water, melt on the graphene surface. At sufficiently high concentrations, the unfolded RNA molecules form a film that entraps nanobubbles; at lower concentrations, they assemble into clusters of unfolded RNA oligonucleotides that are sparsely distributed over graphene surface. The calculations suggested that the experimentally observed unfolding occurs because stacking interactions between RNA nucleobases and graphene outweigh the intramolecular interactions that stabilize the RNA hairpin in water. The height and distribution of nanobubbles over the graphene surface depended on the number of graphene layers, i.e. the hydrophobicity of the graphene surface. On single layer graphene, the bubbles were smaller and more densely distributed, while on graphite they were large and sparsely distributed over the surface. Biomacromolecules can thus display very specific behaviors upon contact with graphene surfaces in water, and their properties can vary with the surface hydrophobicity, concentration and temperature. These results and the implied possibility of manipulating the properties of surface-bound biomolecules should be borne in mind when developing graphene-based sensors or graphene-based nanocarriers for applications in areas such as drug delivery or gene therapy.

ORCID iDs

S Zhang ⓘ https://orcid.org/0000-0003-0170-6470
M Dong ⓘ https://orcid.org/0000-0002-2025-2171
M Otyepka ⓘ https://orcid.org/0000-0002-1066-5677

References

[1] Schedin F, Geim A K, Morozov S V, Hill E W, Blake P, Katsnelson M I and Novoselov K S 2007 *Nat. Mater.* **6** 652–5
[2] Shao Y, Wang J, Wu H, Liu J, Aksay I A and Lin Y 2010 *Electroanalysis* **22** 1027–36
[3] Pumera M, Ambrosi A, Bonanni A, Chng E L K and Poh H L 2010 *TrAC Trends Anal. Chem.* **29** 954–65
[4] Georgakilas V, Otyepka M, Bourlinos A B, Chandra V, Kim N, Kemp K C, Hobza P, Zbořil R and Kim K S 2012 *Chem. Rev.* **112** 6156–214
[5] Liu Y, Dong X and Chen P 2012 *Chem. Soc. Rev.* **41** 2283–307
[6] Traversi F, Raillon C, Benameur S M, Liu K, Khlybov S, Tosun M, Krasnozhon D, Kis A and Radenovic A 2013 *Nat. Nanotechnol.* **8** 939–45
[7] Dontschuk N *et al* 2015 *Nat. Commun.* **6** 6563
[8] Yang K, Feng L, Shi X and Liu Z 2013 *Chem. Soc. Rev.* **42** 530–47
[9] Venkatesan B M and Bashir R 2011 *Nat. Nanotechnol.* **6** 615–24

[10] Xie P, Xiong Q, Fang Y, Qing Q and Lieber C M 2012 *Nat. Nanotechnol.* **7** 119–25

[11] Min S K, Kim W Y, Cho Y and Kim K S 2011 *Nat. Nanotechnol.* **6** 162–5

[12] Park S Y, Park J, Sim S H, Sung M G, Kim K S, Hong B H and Hong S 2011 *Adv. Mater.* **23** H263–7

[13] Li N *et al* 2011 *Biomaterials* **32** 9374–82

[14] Park D-W *et al* 2014 *Nat. Commun.* **5** 5258

[15] Rajendran A, Endo M and Sugiyama H 2014 *Chem. Rev.* **114** 1493–520

[16] Ares P, Fuentes-Perez M E, Herrero-Galan E, Valpuesta J M, Gil A, Gomez-Herrero J and Moreno-Herrero F 2016 *Nanoscale* **8** 11818–26

[17] Orozco M 2014 *Chem. Soc. Rev.* **43** 5051–66

[18] Karplus M and McCammon J A 2002 *Nat. Struct. Mol. Biol.* **9** 646–52

[19] Šponer J, Banáš P, Jurečka P, Zgarbová M, Kührová P, Havrila M, Krepl M, Stadlbauer P and Otyepka M 2014 *J. Phys. Chem. Lett.* **5** 1771–82

[20] Varghese N, Mogera U, Govindaraj A, Das A, Maiti P K, Sood A K and Rao C N R 2009 *ChemPhysChem* **10** 206–10

[21] Sowerby S J, Cohn C A, Heckl W M and Holm N G 2001 *Proc. Natl Acad. Sci. USA* **98** 820–2

[22] Antony J and Grimme S 2008 *Phys. Chem. Chem. Phys.* **10** 2722–9

[23] Gowtham S, Scheicher R, Ahuja R, Pandey R and Karna S 2007 *Phys. Rev.* B **76** 2–5

[24] Spiwok V, Hobza P and Řezáč J 2011 *J. Phys. Chem. C* **115** 19455–62

[25] Patil A J, Vickery J L, Scott T B and Mann S 2009 *Adv. Mater.* **21** 3159–64

[26] Husale B S, Sahoo S, Radenovic A, Traversi F, Annibale P and Kis A 2010 *Langmuir* **26** 18078–82

[27] Zhao X, Striolo A and Cummings P T 2005 *Biophys. J.* **89** 3856–62

[28] Zhao X and Johnson J K 2007 *J. Am. Chem. Soc.* **129** 10438–45

[29] Bobadilla A D and Seminario J M 2011 *J. Phys. Chem. C* **115** 3466–74

[30] Nandy B, Santosh M and Maiti P K 2012 *J. Biosci.* **37** 457–74

[31] Akca S, Foroughi A, Frochtzwajg D and Postma H W C 2011 *PLoS One* **6** e18442

[32] Zhao X 2011 *J. Phys. Chem. C* **115** 6181–9

[33] Fontes G N and Neves B R A 2005 *Langmuir* **21** 11113–8

[34] Carthew R W and Sontheimer E J 2009 *Cell* **136** 642–55

[35] Doherty E A, Batey R T, Masquida B and Doudna J A 2001 *Nat. Struct. Mol. Biol.* **8** 339–43

[36] Nissen P, Ippolito J A, Ban N, Moore P B and Steitz T A 2001 *Proc. Natl Acad. Sci. USA* **98** 4899–903

[37] Antao V P, Lai S Y and Tinoco J I 1991 *Nucl. Acids Res.* **19** 5901–5

[38] Heus H A and Pardi A 1991 *Science* **253** 191

[39] Van Der Spoel D, Lindahl E, Hess B, Groenhof G, Mark A E and Berendsen H J C 2005 *J. Comput. Chem.* **26** 1701–18

[40] Tribello G A, Bonomi M, Branduardi D, Camilloni C and Bussi G 2014 *Comput. Phys. Commun.* **185** 604–13

[41] Correll C C, Beneken J, Plantinga M J, Lubbers M and Chan Y L 2003 *Nucl. Acids Res.* **31** 6806–18

[42] Kührová P, Banáš P, Best R B, Šponer J and Otyepka M 2013 *J. Chem. Theory Comput.* **9** 2115–25

[43] Cheng A and Steele W A 1990 *J. Chem. Phys.* **92** 3858–66

[44] Zgarbová M, Otyepka M, Šponer J, Mládek A, Banáš P, Cheatham T E and Jurečka P 2011 *J. Chem. Theory Comput.* **7** 2886–902

[45] Steinbrecher T, Latzer J and Case D A 2012 *J. Chem. Theory Comput.* **8** 4405–12

[46] Kührová P, Best R B, Bottaro S, Bussi G, Šponer J, Otyepka M and Banáš P 2016 *J. Chem. Theory Comput.* **12** 4534–48

[47] Izadi S, Anandakrishnan R and Onufriev A V 2014 *J. Phys. Chem. Lett.* **5** 3863–71

[48] Joung I S and Cheatham T E 2008 *J. Phys. Chem.* B **112** 9020–41

[49] Hess B, Bekker H, Berendsen H J C and Fraaije J G E M 1997 *J. Comput. Chem.* **18** 1463–72

[50] Bussi G, Donadio D and Parrinello M 2007 *J. Chem. Phys.* **126** 014101

[51] Pérez-Villa A, Darvas M and Bussi G 2015 *Nucl. Acids Res.* **43** 8725–34

[52] Lohse D and Zhang X 2015 *Rev. Mod. Phys.* **87** 981–1035

[53] Seddon J R T, Zandvliet H J W and Lohse D 2011 *Phys. Rev. Lett.* **107** 116101

[54] Mohan S, Hsiao C, Bowman J C, Wartell R and Williams L D 2010 *J. Am. Chem. Soc.* **132** 12679–89

[55] Sheehy J P, Davis A R and Znosko B M 2010 *RNA* **16** 417–29

[56] Rafiee J, Mi X, Gullapalli H, Thomas A V, Yavari F, Shi Y, Ajayan P M and Koratkar N 2012 *Nat. Mater.* **11** 217–22

[57] Shih C-J, Strano M S and Blankschtein D 2013 *Nat. Mater.* **12** 866–9